



Hot Deformation Characterization of Homogenized Mg-Gd-Y-Zn-Zr Alloy During Isothermal Compression

BING LI,¹ BUGANG TENG,^{1,2,3} and WENCHEN XU¹

1.—School of Materials Science and Engineering, Harbin Institute of Technology, Harbin 150001, China. 2.—National Key Laboratory for Precision Hot Processing of Metals, Harbin Institute of Technology, Harbin 150001, China. 3.—e-mail: bgteng@hit.edu.cn

The article investigates the hot deformation behavior of a homogenized Mg-13Gd-4Y-2Zn-0.6Zr (GWZK1342) alloy based on isothermal compression tests. The hot deformation characterization of the GWZK1342 alloy was investigated through the work-hardening rate θ and the inflection point of $\ln \theta - \varepsilon$ curves; thus, the critical strain model was established. Furthermore, the hot deformation map was formulated based on the critical strain, steady strain and variation of power dissipation at different deformation parameters. The optimum parameters can be determined as the process parameters corresponding to the value of $\ln Z < 40$, and the dynamic recrystallization (DRX) predominately operates to accommodate plastic deformation. The kink mechanism of the long period-stacking ordered (LPSO) phase predominately operates as $\ln Z$ exceeds 43. The broken lamellar 14H-LPSO phase can facilitate continuous DRX because of the reduced inhibition effect on lattice rotation and promote discontinuous DRX nucleation through a particle-stimulated nucleation (PSN) mechanism as $\ln Z$ is < 40 .

INTRODUCTION

Recently, demand for wide application of magnesium alloys has been increasing because of their favorable properties and high specific strength.^{1–4} However, the promoted application of the magnesium alloy was limited because of poor formability caused by the limited number of basal slip systems under ambient temperature.^{5–7} The plasticity of the magnesium alloy can be improved by elevating the deformation temperature, which can be attributed to increasing the number of slip planes and reducing the critical shear stress of the non-basal plane slip.^{4,8} Considerable research has concluded that the addition of rare earth elements to magnesium alloys can contribute to better mechanical properties than conventional magnesium alloys because of the disperse precipitation of the second rare element phase, which can inhibit the diffusion of the matrix phase and movement of dislocation.^{9–12} Many researchers have concluded that the formation of the long period-stacking order (LPSO) phase can contribute to improving the mechanical properties of Mg-Y-Zn alloys, which was associated with the constant atomic Y/Zn.¹³ Hagiwara et al.^{14,15}

discovered that the LPSO phase can severely hinder the non-basal slip systems, and Yamasaki et al.¹⁶ proposed that the kink band of the LPSO phase was the major characteristic of the microstructure evolution within the Mg-Zn-Y alloy.

The thermomechanical process was mostly conducted on the magnesium alloy containing RE elements because of the poor plasticity at ambient temperature. The dynamic recrystallization (DRX) operates during the thermomechanical process, which was closely related to the deformation temperature, strain rate, accumulative strain and initial microstructure. Zhang et al.¹⁷ investigated the DRX behavior of the Mg-4Y-2Nd-0.2Zn-0.5Zr alloy during hot compression and proposed that the dynamically precipitated particles facilitated the continuous dynamic recrystallization (CDRX) of as-solution samples. Xiao¹⁸ studied the DRX behavior of the Mg-8.3Gd-2.6Y-0.4Zr alloy and concluded that DRX sites would transfer from the twin boundaries to initial grain boundaries gradually with increasing temperature or decreasing strain rate. Xu¹⁹ proposed that the DRX and addition of RE elements could reduce the basal texture intensity of the hot-rolled Mg-Gd-Y-Zn-Zr alloy. Several

studies have concluded that the LPSO phase within the α -Mg grains can effectively hinder the DRX process at lower accumulative strain and accommodate the plastic strain through the kink mechanism. However, a few studies have investigated the effect of a broken LPSO phase on the microstructure evolution during isothermal compression. Thus, it is significant to investigate the effect of the LPSO phase on microstructure evolution at different process parameters and construct a more accurate characterization method for process parameters.

The article investigates the critical strain for the DRX of Mg-13Gd-4Y-2Zn-0.6Zr at various process parameters. Furthermore, the hot deformation map was constructed to investigate the isothermal compression behavior of the Mg-Gd-Y-Zn-Zr alloy, which can more accurately demonstrate the deformation mechanism at different process parameters. The microstructure observations corresponding to different process parameters were conducted to investigate the effect of the LPSO phase on the deformation mechanism and microstructure evolution at different $\ln Z$ values.

EXPERIMENTAL MATERIAL AND PROCEDURE

The material employed in the present study was the Mg-13Gd-4Y-2Zn-0.6Zr (GWZK1342) alloy. The GWZK1342 alloy was homogenized at 793 K for 12 h to eliminate the eutectic phase at grain boundaries. Figure 1 demonstrates the optical microstructure of the homogenized GWZK1342 alloy. As Fig. 1 illustrates, the homogenized GWZK1342 alloy demonstrates the α -Mg matrix and the interdendritic block-shaped $\text{Mg}_{12}(\text{Gd,Y})\text{Zn}$ phase with a 14H-LPSO structure, which was transformed from the interdendritic 18R-LPSO.²⁰ The intragranular lamellar-shaped 14H-LPSO phase precipitated and grew across the whole grains during the homogenization process, which was identified as the $\text{Mg}_{12}(\text{Gd,Y})\text{Zn}$ phase.²⁰ The LPSO

phase can accommodate the plastic deformation through its kinking mechanism, which can improve the mechanical properties of the alloy.²¹

The homogenized GWZK1342 alloy was electrical discharge machined to cylinder specimens with height of 12 mm and diameter of 8 mm. The compression tests were carried out on the Gleeble-1500D thermal-mechanical simulator, and the graphite sheets were selected as the lubricant to decrease the effect of interfacial friction between the contact surfaces. The samples were electrochemical polished to eliminate the effect of oxide before compression testing. The experimental temperatures were set to 673 K, 698 K, 723 K and 748 K, and the initial strain rates were set to 0.001 s^{-1} , 0.01 s^{-1} , 0.1 s^{-1} and 1 s^{-1} . The samples were finally compressed to height engineering reduction of 60% to obtain a total strain of 0.9 with protective atmosphere. Furthermore, isothermal compression tests with strains of 0.2, 0.4 and 0.6 were conducted at 748 K and 0.001 s^{-1} to investigate the deformation mechanism. The specimens were heated up to the deformed temperature at a heating rate of 5 K s^{-1} and retained for 2 min to obtain temperature homogenization. The specimens were quenched with water immediately at the end of compression tests to reserve the microstructure. The specimens for microstructure analysis were selected in the center region parallel to the compression axis. The etching solution for the compressed samples was an acetic picral etchant (5 g picric acid, 5 ml alcohol, 100 ml acetic acid and 10 ml distilled water). The microstructure after hot compression was observed through the Leica optical microscope. The electron backscatter diffraction (EBSD) examination was conducted on the *Carl Zeiss Merlin Compact*, equipped with an EBSD system. The specimens for EBSD observation were prepared by electro-polishing at voltage of 3.0 V and 248 K in the solution of perchloric acid and alcohol with the volume ratio of 1:9. The EBSD results were collected with scanning step size of $1.2 \mu\text{m}$. The TEM observations were also conducted, and the bright field images were obtained.

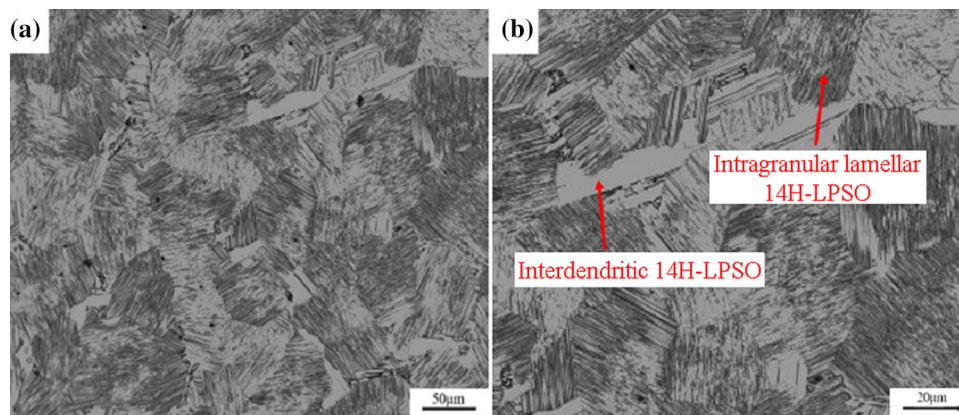


Fig. 1. The optical microstructure of the homogenized Mg-13Gd-4Y-2Zn-0.6Zr alloy: (a) $\times 200$ (b) $\times 500$.

RESULTS

Flow Stress Behavior

Figure 2a–d shows the true stress versus true strain of the GWZK1342 alloy at a strain rate of 0.001–1 s⁻¹ and temperature of 673–748 K. As demonstrated in Fig. 2, the flow stress initially increases significantly with further strain at the early deformation stage, which is attributed to work hardening caused by dislocation generation and multiplication. Then, the flow stress reaches the peak value and declines subsequently, which can be explained by the dynamic softening resulting from DRX dominating over the work hardening. The driving force of DRX increases by dislocation accumulation, and eventually DRX initializes at a critical strain. Subsequently, the flow stress tends to reach a steady state with further strain, which was due to the dynamic equilibrium between work hardening and dynamic softening induced by DRX. However, as the temperature exceeds 698 K at the strain rate of 1 s⁻¹, the flow stress curves demonstrate multiple peaks. Jiang²² ascribed it to the fast grain boundary migration rate and fast nucleation and growth of the recrystallization grain at higher strain rate. Obviously, the flow stress decreases significantly and the peak strain declines at a lower strain rate ($\dot{\epsilon} = 0.01 \text{ s}^{-1}$ and $\dot{\epsilon} = 0.001 \text{ s}^{-1}$) or elevated temperature (723 K and 748 K). The elevated temperature and lower strain rate can facilitate the dislocation movement and annihilation, and the higher migration of grain boundaries,²³ which result in the reduction of flow stress. Meanwhile, the elevated temperature can result in lower critical resolved shear stress (CRSS) for a basal and non-basal slip system, which can explain the reason for lower flow stress at elevated temperature. Furthermore, the elevated temperature and reduced strain rate contribute to the initiation of DRX at lower strain, and the DRX softening effect is sufficient to

counterbalance the work-hardening effect at lower strain; thus, the peak strain declines as the strain rate reduces or deformation temperature increases.

Determination of Material Constants

Previous studies have concluded that the Zener–Hollomon parameter (Z) can depict the effects of strain rate and temperature on the flow stress behavior.^{24–27} These are typically expressed as:^{4,21,28–30}

$$Z = \dot{\epsilon} \exp\left(\frac{Q}{RT}\right) \tag{1}$$

$$\dot{\epsilon} = AF(\sigma) \exp\left(-\frac{Q}{RT}\right) \tag{2}$$

$$F(\sigma) = \begin{cases} \sigma^n & \alpha\sigma < 0.8 \\ \exp(\beta\sigma)\alpha\sigma & \alpha\sigma > 1.2 \\ [\sinh(\alpha\sigma)]^n & \text{for all } \sigma \end{cases} \tag{3}$$

where Q is the activation energy of hot deformation (kJ mol⁻¹), which indicates the difficulty of plastic deformation. σ is the flow stress (MPa), $\dot{\epsilon}$ is the strain rate (s⁻¹), R is the universal gas content (8.314 J mol⁻¹ K⁻¹), and T is the absolute temperature (K). A , α , β , n are the material constants. The stress multiplier α is defined as $\alpha = \beta/n$. As an example, the true strain of 0.1 is first considered in the solution process of the material constants.

For the low stress level ($\alpha\sigma < 0.8$) and high stress level ($\alpha\sigma > 1.2$), substituting Eq. 3 into Eq. 2, as shown in Eqs. 4 and 5, respectively, can illustrate the relationship between the stress and strain rate.

$$\dot{\epsilon} = A'\sigma'^{n1} \text{ (for } \alpha\sigma < 0.8) \tag{4}$$

$$\dot{\epsilon} = A''\exp(\beta\sigma) \text{ (for } \alpha\sigma > 1.2) \tag{5}$$

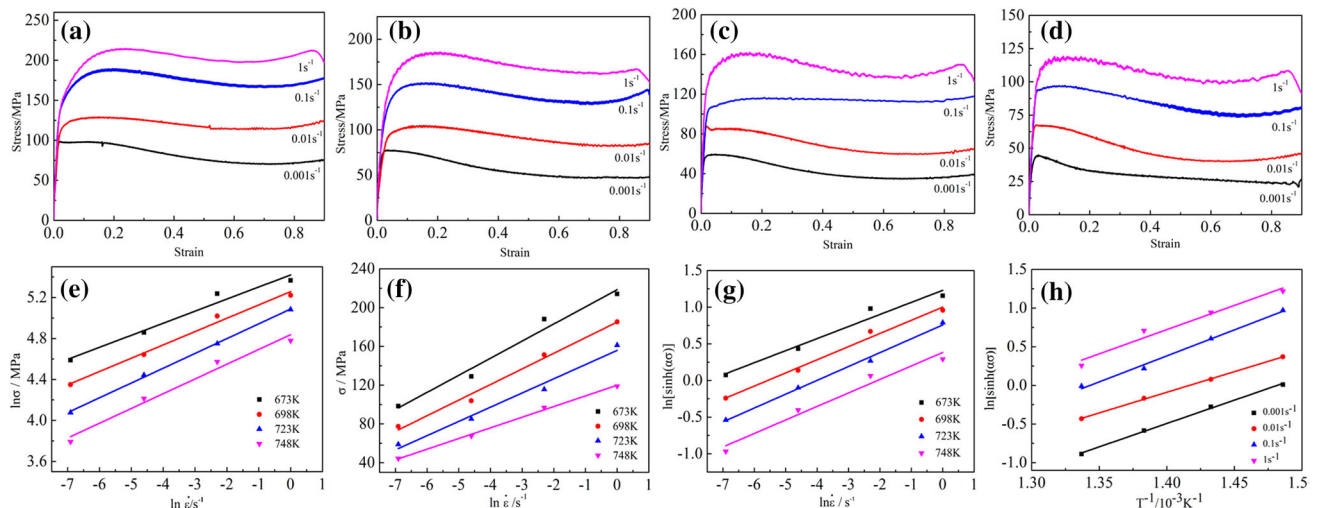


Fig. 2. The true stress versus true strain at various strain rates and temperatures of (a) 673 K, (b) 698 K, (c) 723 K, (d) 748 K and the relationship between (e) $\ln \dot{\epsilon}$ and $\ln \sigma$; (f) $\ln \dot{\epsilon}$ and σ . (g) The curves of $\ln[\sinh(\alpha\sigma)] - \ln \dot{\epsilon}$; (h) the curves of the $\ln[\sinh(\alpha\sigma)]$ versus T^{-1} .

where A' and A'' are material parameters. Taking the natural logarithms of both sides of Eqs. 4 and 5 conforms to the following equations:

$$\ln \sigma = \frac{1}{n_1} \ln \dot{\varepsilon} - \frac{1}{n_1} \ln A' \quad (6)$$

$$\sigma = \frac{1}{\beta} \ln \dot{\varepsilon} - \frac{1}{\beta} \ln A'' \quad (7)$$

Then, the strain rates and corresponding flow stresses at different deformation temperatures were substituted into Eqs. 6 and 7, thus obtaining the slopes of $\ln \sigma - \ln \dot{\varepsilon}$ and $\sigma - \ln \dot{\varepsilon}$, as demonstrated in Fig. 2e and f, and the values of n_1 and β can be determined from the mean slope of the $\ln \sigma - \ln \dot{\varepsilon}$ and $\sigma - \ln \dot{\varepsilon}$ plot. Therefore, the average values of n_1 and β are calculated as 7.6493 and 0.0731 MPa⁻¹, respectively. Then, α was calculated to be 0.009552 through the above equation.

Then, substituting Eq. 3 into Eq. 2, Eq. 2 can be demonstrated as follows for all stress levels:

$$\dot{\varepsilon} = A[\sinh(\alpha\sigma)]^n \exp\left(-\frac{Q}{R_0T}\right) \quad (8)$$

Differentiating Eq. 8 at a particular strain rate, the deformation activation energy Q can be expressed as follows:

$$Q = R_0 \left[\frac{\partial \ln \dot{\varepsilon}}{\partial \ln[\sinh(\alpha\sigma)]} \right]_T \left[\frac{d \ln[\sinh(\alpha\sigma)]}{dT^{-1}} \right]_{\dot{\varepsilon}} \quad (9)$$

Substituting the values of temperature and flow stress into Eq. 9, and the slopes of the lines of $\ln[\sinh(\alpha\sigma)] - \ln \dot{\varepsilon}$ and $\ln[\sinh(\alpha\sigma)] - T^{-1}$ can be calculated, as shown in Fig. 2g and h. Then, the average Q value can be calculated to be 276.2141 kJ mol⁻¹, which is much higher than the self-diffusion activation energy of pure magnesium alloy 135 kJ mol⁻¹. The high Q value can be ascribed to the inhibition effect of the 14H-LPSO phase on lattice rotation²⁰ and low diffusivity of heavy Gd and Y elements.¹⁷

Critical Strain Prediction Model

The critical strain ε_c for the initiation of DRX can be calculated through the inflection point of work hardening rate θ versus flow stress σ ; thus, the ε_c can be determined through the equation $-\frac{\partial^2 \theta}{\partial \varepsilon} = 0$. Figure 3a demonstrates the $\ln \theta - \varepsilon$ curves at a constant strain rate of 0.01 s⁻¹ from 673 K to 748 K, and the inflection point position corresponds to the critical strain. Similarly, Fig. 3b illustrates the curves of $\ln \theta - \varepsilon$ for a constant temperature of 698 K at 0.001-1 s⁻¹. Furthermore, the detailed values of critical strain and steady-state strain at different temperatures and strain rates are presented in Table I. The results illustrate that the critical strain and steady-state strain are elevated

as the $\ln Z$ increases, which indicates that the driving force for DRX declines with increasing $\ln Z$.

The critical strain model can be formulated to investigate relations between the deformation parameters and the critical strain for the initiation of DRX. By introducing the Sellers model, the critical strain model can be expressed as model I³¹:

$$\varepsilon_c = aZ^b \quad (10)$$

Then, by taking the logarithm of both sides of Eq. 10, the ε_c can be depicted as:

$$\ln \varepsilon_c = \ln a + b \ln Z \quad (11)$$

The values of a and b can be obtained from the intercept and slope of Fig. 3c; thus, the critical strain model can be demonstrated as: $\varepsilon_c = 3.65 \times 10^{-5} Z^{0.1725}$. Furthermore, the average absolute relative error (AARE), correlation coefficient (R) and root mean square error (RMSE) were utilized to evaluate the critical strain model. They can be expressed as follows:

$$AARE(\%) = \frac{1}{N} \sum_{i=1}^N \left| \frac{\sigma_e^i - \sigma_p^i}{\sigma_e^i} \right| \times 100 \quad (12)$$

$$R = \frac{\sum_{i=1}^n (\sigma_e^i - \bar{\sigma}_e) (\sigma_p^i - \bar{\sigma}_p)}{\sqrt{\sum_{i=1}^n (\sigma_e^i - \bar{\sigma}_e)^2} \sqrt{\sum_{i=1}^n (\sigma_p^i - \bar{\sigma}_p)^2}} \quad (13)$$

$$RMSE = \sqrt{\frac{1}{N} \sum_{i=1}^N (\sigma_e^i - \sigma_p^i)^2} \quad (14)$$

Thus, the AARE, R and RMSE of the critical strain model can be calculated to be 3.52%, 0.982 and 0.104, respectively. Furthermore, Yu et al. proposed another critical strain characterization model containing Z parameters, which was denoted as model II:³²

$$\varepsilon_c = abZ^R \quad (15)$$

By mathematical operation, ε_c can be demonstrated as:

$$\ln \varepsilon_c = y_0 + k \times e^{R \ln Z} \quad (16)$$

Then, the value of y_0 , k , and R can be fitted to be -7.029, 0.751 and 0.041, respectively, and the critical strain model can also be expressed as follows:

$$\varepsilon_c = 8.8582 \times 10^{-4} \cdot 2.1191 Z^{0.041}$$

Besides, the AARE, R and RMSE of the latter critical strain model can be calculated to be 5.02%, 0.961 and 0.1183, respectively, as demonstrated in Fig. 3d. Figure 3 shows that model I possesses higher prediction accuracy than model II.

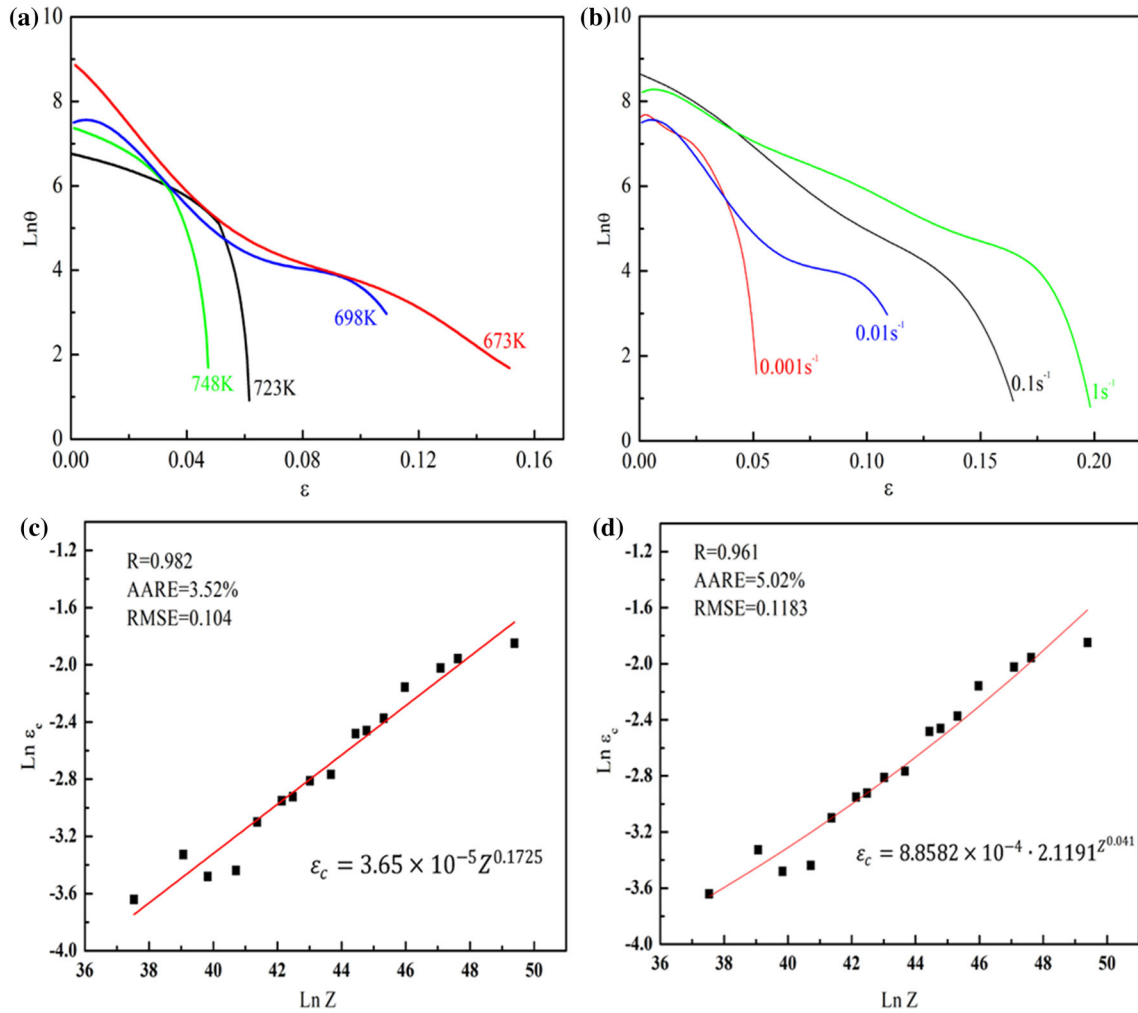


Fig. 3. Relationship between (a) $\ln \theta - \epsilon$ curves at 0.01 s^{-1} and (b) $\ln \theta - \epsilon$ curves at 698 K and relationship between $\ln \epsilon_c$ and $\ln Z$ (c) model I and (d) model II.

Table I. The critical strain and steady-state strain at different deformation parameters

Deformation temperature/K	Strain rate/ s^{-1}	$\ln Z$	Critical Strain	Steady-state strain
748	0.001	37.5290	0.0262	0.41097
723	0.001	39.0656	0.0359	0.4915
748	0.01	39.8316	0.0308	0.5394
698	0.001	40.7122	0.0321	0.5541
723	0.01	41.3682	0.0451	0.5741
748	0.1	42.1343	0.0523	0.6004
673	0.001	42.4812	0.0538	0.6105
698	0.01	43.0148	0.0601	0.6398
723	0.1	43.6708	0.0629	0.64
748	1	44.4369	0.0836	0.6642
673	0.01	44.7838	0.0854	0.6199
698	0.1	45.3174	0.0932	0.6418
723	1	45.9733	0.1157	0.6345
673	0.1	47.0864	0.1323	0.6456
698	1	47.6204	0.1414	0.6702
673	1	49.3890	0.1574	0.6757

Power Dissipation Map

The power dissipation map can characterize the microstructure evolution during the hot deformation process. The relationship between heat generations from plastic deformation and the rate of energy dissipation with microstructure evolution can be characterized through the dynamic material model (DMM). Based on the DMM, the total power (P) can be depicted as:^{33,35}

$$P = G + J = \sigma \dot{\epsilon} = \int_0^{\dot{\epsilon}} \sigma d\dot{\epsilon} + \int_0^{\sigma} \dot{\epsilon} d\sigma \quad (17)$$

where the G represents the dissipation energy stemming from plastic deformation and J represents the power dissipation associated with the microstructural changes.^{33–35}

For the supplied strain and temperature, based on the constitutive flow behavior equation $\sigma = K\dot{\epsilon}^m$, the value of m can be expressed as:

$$m = \frac{\partial J}{\partial G} = \frac{\dot{\epsilon} \partial \sigma}{\sigma \partial \dot{\epsilon}} = \frac{\partial(\ln \sigma)}{\partial(\ln \dot{\epsilon})} \Big|_{\epsilon, T} \quad (18)$$

For the given deformation temperature and strain, through incorporating Eq. 17, the J can be expressed as:

$$J = \sigma \dot{\epsilon} - \int_0^{\dot{\epsilon}} K \dot{\epsilon}^m d\dot{\epsilon} = \frac{m}{m+1} \sigma \dot{\epsilon}$$

The value of J reaches its maximum at $m = 1$, and $J_{\max} = \frac{\sigma \dot{\epsilon}}{2}$. The efficiency of power dissipation η can be defined as:

$$\eta = \frac{J}{J_{\max}} = \frac{2m}{m+1} \quad (19)$$

Constructing the power dissipation maps by plotting temperature-strain rate contours at different strains, as shown in Fig. 4a–c. The traditional power dissipation map can only optimize the parameters respectively at certain strains; however, the microstructure evolution with strain cannot be characterized through the power dissipation map. The efficiency variation of power dissipation can reflect the microstructure evolution during the thermomechanical process. The efficiency variation of power dissipation versus strain at different values of $\ln Z$ is illustrated in Fig. 4d–f. It is documented that the efficiency of power dissipation for DRX is only 30–40% for the low stacking fault energy, such as the magnesium alloy.^{36,37} For the value of $\ln Z < 40$, the efficiency of power dissipation η exceeds 0.35 at the strain of 0.2 and then declines or increases slightly with further strain, which indicates that DRX grain nucleation starts at lower strain and DRX contributes more to a higher value of η at a strain of 0.2. Then, the decline and slight increase of η can be ascribed to the

microstructure evolving slightly and DRX contributing little to the microstructure evolution. For $40 < \ln Z < 43$, the η is < 0.30 at the strain of 0.2 and then increases with strain increasing, which illustrates that DRX initiates at higher strain and moderately promotes microstructure evolution. For $\ln Z > 43$, the value of η is < 0.30 from lower strain to higher strain; thus, the DRX marginally facilitates the microstructure evolution during isothermal compression.

The power dissipation maps can demonstrate the optimum process parameters at a certain strain; however, the strain and microstructure evolution were not characterized in the processing maps. By incorporating the strain with the efficiency of power dissipation, the hot deformation maps can be formulated based on the critical strain, steady-state strain and efficiency variation of power dissipation at different values of $\ln Z$, as shown in Fig. 4g. The feature of microstructure corresponding to different deformation parameters can be predicted through the hot deformation map. For $\ln Z < 40$, the efficiency of power dissipation exceeds 0.35 and DRX initializes at lower strain; thus, DRX may predominately operate to accommodate the plastic deformation. For $40 < \ln Z < 43$, the efficiency of power dissipation is low at lower strain and then increases with further strain, and the limited fraction of DRX grains may be observed at corresponding process parameters. Furthermore, the marginal fraction of the DRX microstructure may be obtained at process parameters corresponding to $\ln Z > 43$ because of the slight variation of lower power dissipation efficiency.

Microstructure Observation

Figure 5a–c illustrates the optical microstructure corresponding to domain I (shown in Fig. 4g) at different values of $\ln Z$. The numerous DRX grains can be observed at corresponding parameters, which demonstrate that the DRX predominately operates as the value of $\ln Z$ below 40. Furthermore, the zigzagged and broken 14H-LPSO phases were observed at corresponding parameters, as demonstrated in Fig. 5a and b. Zhou²³ proposed that the crushed 14H-LPSO phase can reduce the inhibition effect on the lattice rotation and facilitate the operation of CDRX. The compression tests at 748 K and strain rate of 0.001 s^{-1} with different strains were conducted to illustrate the DRX nucleation mechanism.

Figure 5e–m demonstrates the inverse pole figure (IPF) maps and grain orientation spread (GOS) maps with different strains at a temperature of 748 K and strain rate of 0.001 s^{-1} , which corresponds to the $\ln Z$ of 37.529. The GOS can demonstrate the average difference of orientation between the average grain orientation and all points within a grain, which can be illustrated as:^{37,38}

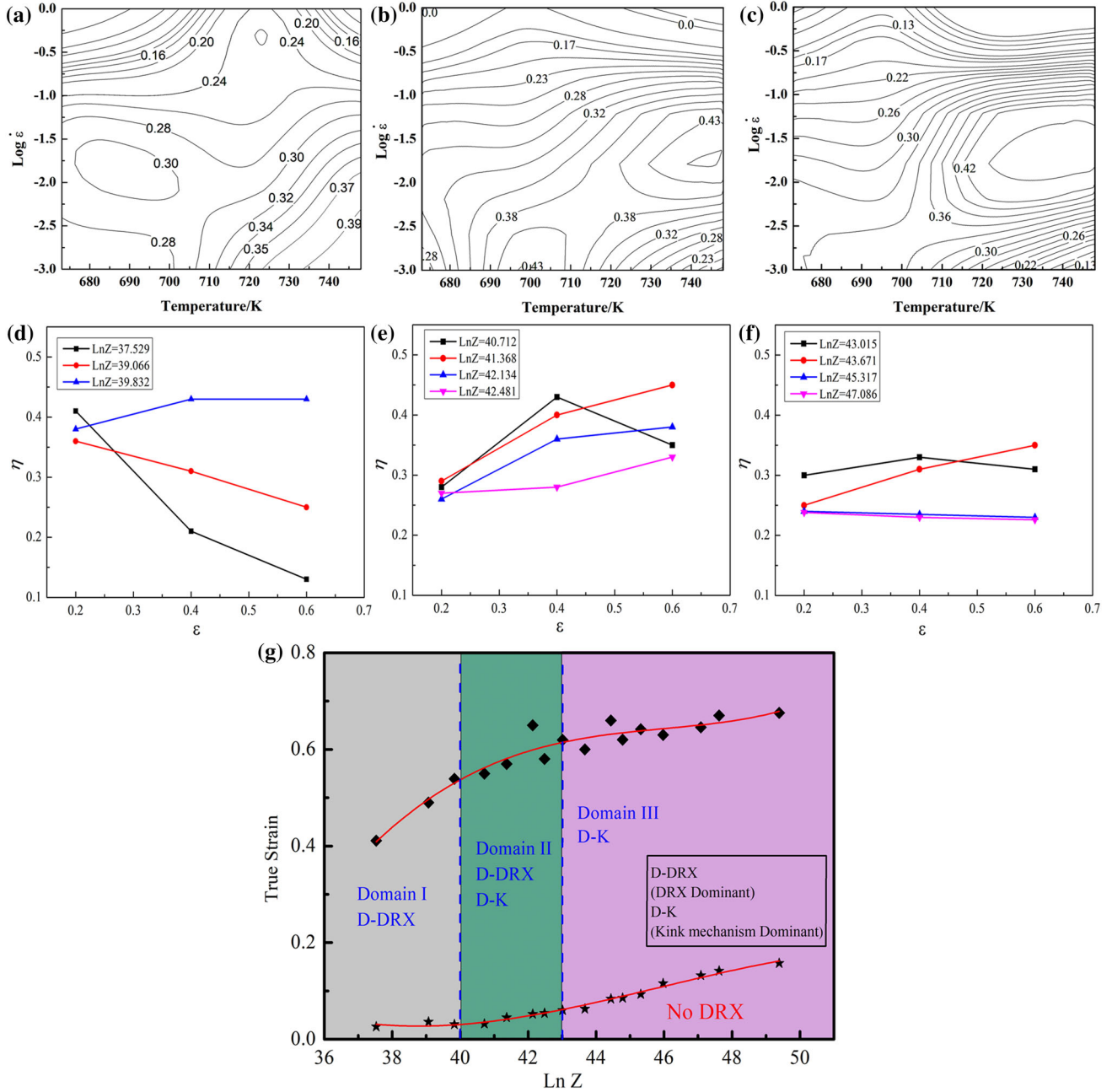


Fig. 4. Power dissipation map at strains of (a) 0.2, (b) 0.4 and (c) 0.6; variation of power dissipation versus strain at values of $\ln Z$ (d), $\ln Z < 40$, (e) $40 < \ln Z < 43$, (f) $\ln Z > 43$ and (g) hot deformation map.

$$\text{GOS} = \frac{1}{N} \sum_{A=1}^N \left\{ \min \left[\cos^{-1} \left(\frac{\text{trace} [g_{ave} (h_i g^A) - 1]}{2} \right) \right] \right\} \quad (20)$$

where A represents the A th point within a grain, N is the total measured points within a grain, g_{ave} represents the average orientation of all points within a grain, g^A represents the orientation of the A th point, and h_i represents the minimum orientation difference between the measured point and the

average orientation.³⁷ The GOS threshold value of DRX can be determined as 2° for the homogenized GWZK1342 alloy.³⁷

The blank regions in the IPF maps and GOS maps mainly indicate the LPSO phase, which was difficult to recognize in the EBSD system because of a negligible confidence index (CI) resulting from the absence of corresponding parameters. At lower strain, the primary α -Mg grains were surrounded by the finer DRX grains at grain boundaries. The addition of the element Zn contributes to the formation of the 14H-LPSO phase, which results

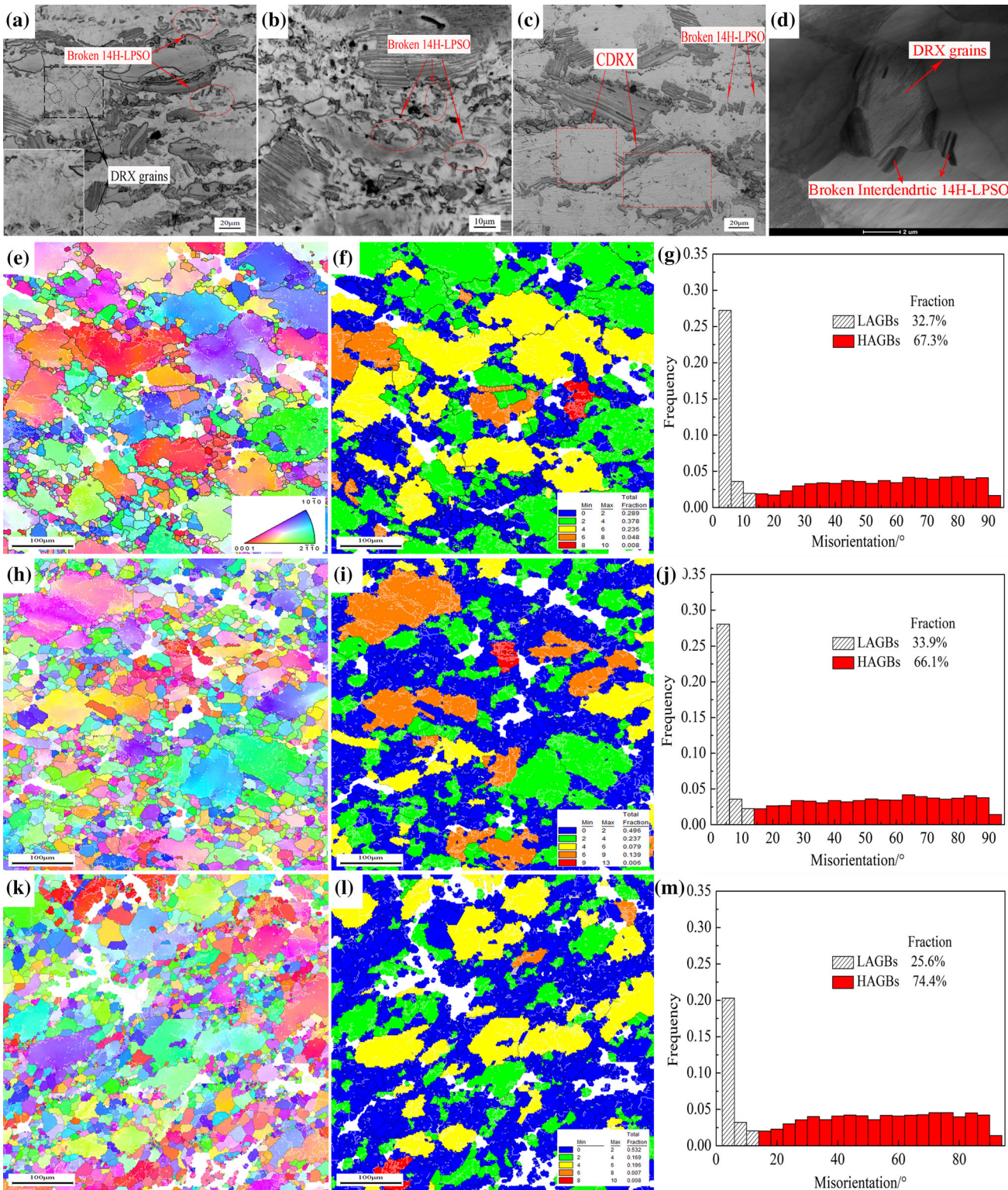


Fig. 5. The microstructure corresponding to domain I at different In Z values: (a) In Z = 37.529 at strain of 0.9; (b) In Z = 39.066 at strain of 0.9; (c) In Z = 37.529 at strain of 0.6; (d) TEM bright field image of DRX grains with strain of 0.6 at In Z = 37.529 and IPF maps with strain of (e) 0.2, (h) 0.4 and (k) 0.6. GOS maps with strain of (f) 0.2, (i) 0.4 and (l) 0.6 at In Z = 37.529 and the fraction of LAGBs and HAGBs of (g) 0.2, (j) 0.4 and (m) 0.6.

in the low stacking energy of the magnesium alloy containing RE elements. The dislocations were hard to slide and climb because of the low stacking

energy, and thus dynamic recovery (DRV) was difficult to operate. Furthermore, the interdendritic 14H-LPSO phase breaks and provides the

nucleation site for DRX; thus, the discontinuous dynamic recrystallization (DDRX) first occurs at the grain boundaries. Figure 5(d) demonstrates the TEM bright field image of the broken interdendritic 14H-LPSO phase and adjacent DRX grains with strain of 0.6 at 475 K, 0.001 s^{-1} . The DRX grains nucleate around the broken 14H-LPSO phase, as marked by the red arrow in Fig. 5d, which indicates that the broken 14H-LPSO phase provides a nucleation site for DRX. As the strain increases, the intragranular 14H-LPSO phase was zigzagged and kinked,²³ which can provide sufficient sites for dislocations to accumulate and cluster. The distinctly oriented finer grains can be observed within the deformed grains, as marked with arrows in Fig. 5k, which indicates that DRX operates within the deformed grains. The climb and rearrangement of high-density dislocations around the kinked lamellar 14H-LPSO phase facilitate the formation of low-angle grain boundaries (LAGBs), and the LAGBs can transform into high-angle grain boundaries (HAGBs) through lattice rotation and incorporation of dislocations. It can be concluded that the kinked lamellar 14H-LPSO phase can facilitate DRX nucleation within the deformed grains. The intragranular lamellar 14H-LPSO phase was prone to be crushed and broken with further strain at higher temperature and lower strain rate. Once the 14H-LPSO phase was crushed, the inhibition effect of the 14H-LPSO phase on the lattice rotation reduced, which could facilitate the CDRX process. Accordingly, numerous LAGBs arose within the deformed grains, indicated by the white lines in Fig. 5e, h, and k. Furthermore, the fraction of LAGBs declined with increasing accumulative strain, as demonstrated in Fig. 5g, j, and m. The LAGBs can transform into HAGBs with further strain by incorporating dislocation and subgrain rotation; thus, CDRX grains form within the deformed grains, as Fig. 5c, e, h and k demonstrate. Besides, the fraction of HAGBs increased with further strain. The area fraction of DRX grains increased from 28.9% to 53.2% with strain increasing from 0.2 to 0.6, as illustrated in Fig. 5f, i and l, and the DRX grains demonstrate a more random orientation.

The microstructures corresponding to domain II at different $\ln Z$ values are demonstrated in Fig. 6a–d. The optical observation demonstrates the bimodal microstructure, and the primary grains were surrounded by finer DRX grains at grain boundaries. The primary grains were distorted and alerted to flat strips perpendicular to the compression direction. The hexagonal, closely packed (HCP) crystal structure of the α -Mg matrix provides limited numbers of slipping systems; thus, the other deformation mechanism can be observed in the magnesium alloy.³² The 14H-LPSO phase can impede the basal dislocation movement; thus, the dislocations pile up at the boundaries between the

LPSO phase and 2H-Mg structure as $a + c$ dislocation starts.³² The stress concentration occurs within the α -Mg grain along the 14H-LPSO phase, and the original lamellar 14H-LPSO phases were bent to accommodate the plastic deformation. The kink band of the 14H-LPSO phase can homogenize the stress field in the primary α -Mg matrix, in which the basal slip predominately operates. Furthermore, the 14H-LPSO phase was not broken at the process parameters corresponding to domain II, which indicates that the 14H-LPSO phase was prone to being easily crushed, zigzagged and broken at a lower value of $\ln Z$ (higher temperature and lower strain rate). The lamellar 14H-LPSO hindered the lattice rotation, and thus the CDRX process was suppressed. The DDRX occurred at the grain boundaries, and the fraction of DRX grains is lower than at process parameters corresponding to domain I. Furthermore, the fraction of DRX grains reduced with an increasing $\ln Z$ value. Thus, the kink mechanism of the 14H-LPSO phase and DDRX mechanism plays a dominant role at process parameters corresponding to $40 < \ln Z < 43$.

The microstructures corresponding to domain III at different $\ln Z$ values are presented in Fig. 6e–h. It can be observed that a limited fraction of DRX grains distribute at the primary grain boundaries, which indicates that DRX marginally facilitates the thermomechanical deformation at corresponding parameters. The primary α -Mg grains were compressed to flat strips, and the kink band of the 14H-LPSO phase can be observed, which indicates that the kink mechanism of the LPSO phase predominately operates to accommodate the stress concentration. Thus, the dynamic softening effects arising from DRX decreased, which can be verified through the stress–strain curves at the corresponding process parameters. Obviously, the fraction of DRX grains declines as the $\ln Z$ value increases because of the lower thermal activation energy for DDRX at a higher $\ln Z$ value (higher strain rate and lower temperature).

DISCUSSION

It is documented that the optimum process parameters can be determined as the parameters corresponding to the maximum efficiency of power dissipation. However, process parameter of 723 K and 0.01 s^{-1} locate in the region of the maximum power dissipation efficiency at strain of 0.4 and 0.6; the corresponding microstructure demonstrates the characteristic of bimodal microstructure rather than the full DRX microstructure, as demonstrated in Fig. 6b. Therefore, the efficiency variation of power dissipation with strain was selected to characterize the microstructure evolution. The process parameters were divided into three domains based on the efficiency variation of power dissipation, and thus the hot deformation map was constructed.

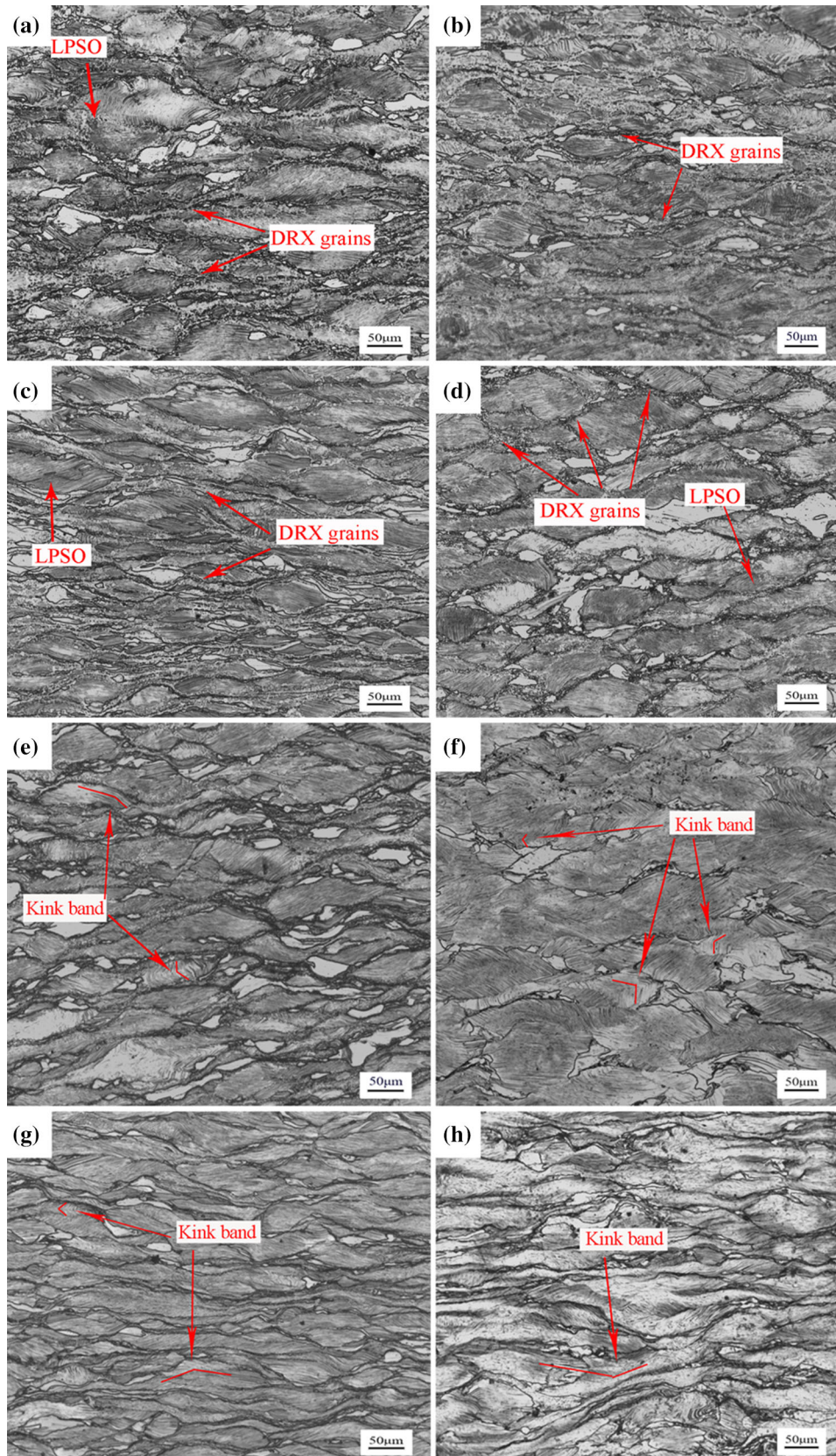


Fig. 6. The microstructures at 0.9 strain with different $\ln Z$ values corresponding to domain II: (a) $\ln Z = 40.712$; (b) $\ln Z = 41.368$; (c) $\ln Z = 42.134$; (d) $\ln Z = 42.4812$. Domain III: (e) $\ln Z = 43.015$; (f) $\ln Z = 43.671$; (g) $\ln Z = 45.317$; (h) $\ln Z = 47.086$.

Considerable studies have demonstrated that the intragranular 14-LPSO phase in the Mg-Gd-Y-Zn-Zr alloy can inhibit the dislocation movement, and thus the DRX process can be impeded.³² Furthermore, the 14H-LPSO phase is sensitive to the deformation temperature and strain rate in this study. The 14H-LPSO phase was zigzagged and broken with further strain at a lower $\ln Z$ value ($\ln Z < 40$). The morphology of the intragranular 14H-LPSO phase can influence the microstructure evolution at different process parameters. From the above information, the efficiency variation of power dissipation η can reveal the microstructure evolution in the thermomechanical process. As illustrated in Fig. 7, DRX facilitates accommodating plastic deformation at a lower $\ln Z$ value (higher temperature and lower strain rate), while the kink mechanism of the 14H-LPSO phase predominately operates at a higher $\ln Z$ value ($\ln Z > 40$). The broken interdendritic 14H-LPSO phase can provide numerous nucleation sites and promote DDRX through the PSN mechanism. Besides, the intragranular 14H-LPSO phase was easily zigzagged and broken at higher temperature and lower strain rate; thus, the inhibition effect of the 14H-LPSO phase on the lattice rotation decreased, which can facilitate the CDRX process. Furthermore, higher temperature and lower strain rates can facilitate dislocation gliding, climbing and sliding, and anchor node dislocation formed easily, which raised the nucleation rate of DDRX.³² Therefore, the broken interdendritic 14H-LPSO phase can contribute to the DDRX through the PSN mechanism, and the broken intragranular 14H-LPSO phase facilitates the CDRX because of the reduced inhibition effect on lattice rotation and dislocation movement. As the temperature declined and strain rate increased, the intragranular 14H-LPSO phase remained, and the dislocations clustered along the 14H-LPSO phase. Thus, the 14H-LPSO phase was bent to

accommodate the stress concentration within the deformed grains for $40 < \ln Z < 43$. CDRX was suppressed because of the inhibition effect of the remaining 14H-LPSO phase on lattice rotation, while DDRX occurred at grain boundaries. For $\ln Z > 43$, the kink mechanism of the 14H-LPSO phase predominately operates to accommodate the dislocation movement and stress concentration resulting from dislocation accumulation reduction, and thus the flow stress declines. However, the basal dislocations re-accumulated along the 14H-LPSO phase with further strain, and thus the flow stress increased. The kink mechanism of the 14H-LPSO phase may be partly responsible for the multiple peaks of flow stress curves at higher strain rate (1 s^{-1}) due to the repeated process described above.

CONCLUSION

The deformation behavior of the homogenized Mg-13Gd-4Y-2Zn-0.6Zr alloy during isothermal compression was investigated through the characterization of DRX behavior and microstructure evolution. The main conclusions can be summarized as follows:

1. The critical strain models for the initiation of DRX were developed based on two different kinds of characterization method. The critical strain model $\varepsilon_c = 3.65 \times 10^{-5} Z^{0.1725}$ can predict the critical strain at different thermomechanical parameters more accurately for the homogenized Mg-13Gd-4Y-2Zn-0.6Zr alloy.
2. The hot deformation map was constructed based on the critical strain, steady-state strain and efficiency variation of power dissipation at different process parameters, which can characterize the microstructure evolution and deformation mechanism at different process parameters. For $\ln Z < 40$, the DRX predominately operates, and the higher fraction of DRX grains can be obtained as strain exceeds the steady strain, and the corresponding process parameters can be determined as the optimum parameters for the hot deformation process of the homogenized Mg-13Gd-4Y-2Zn-0.6Zr alloy.
3. The deformation mechanism varies at different $\ln Z$ values. The DRX mechanism predominately operates at the corresponding parameters for $\ln Z < 40$. The 14H-LPSO phase can be kinked and broken at corresponding process parameters, which facilitates the CDRX because of the reduced inhibition effect on lattice rotation within the α -Mg grains and contributes to the DDRX through the PSN mechanism at grain boundaries. For $40 < \ln Z < 43$, the kink mechanism of the intragranular lamellar 14H-LPSO phase and DDRX at grain boundaries can accommodate the plastic deformation at corresponding parameters. Furthermore, the kink mechanism of the lamellar 14H-LPSO phase is

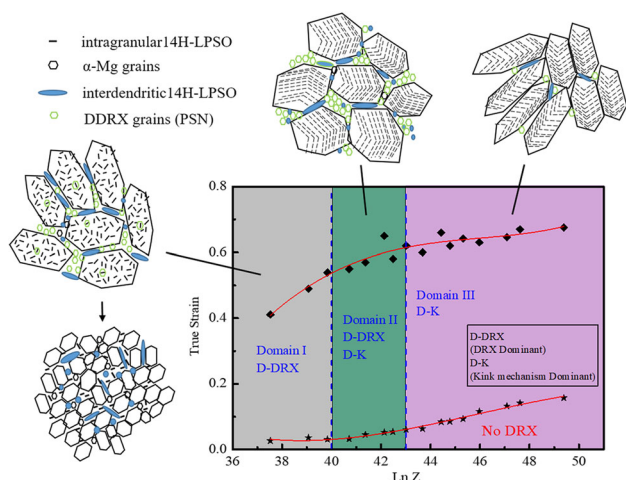


Fig. 7. The schematic diagram of microstructure evolution at different process parameters.

the predominant deformation mechanism for $\ln Z > 43$, which partly results in the multiple peaks of flow stress curves at higher strain rate and elevated temperature.

ACKNOWLEDGEMENTS

This project is supported by the National Natural Science Foundation of China (Grant Nos. 51875127 and 51775137).

REFERENCES

1. L.Q. Wang, R.C. Wang, Y. Feng, M. Deng, and N.G. Wang, *JOM* 69, 2467 (2017).
2. F. Feng, S.Y. Huang, Z.H. Meng, J.H. Hu, Y. Lei, and M.C. Zhou, et al., *Mater. Des.* 57, 10 (2014).
3. W.W. Li, W. Liang, H.X. Wang, and H.W. Guo, *JOM* 69, 2297 (2017).
4. Z.W. Cai, F.X. Chen, and J.Q. Guo, *J. Alloy. Compd.* 648, 215 (2015).
5. H. Mirzadeh, *Mech. Mater.* 77, 80 (2014).
6. P. Maier, R. Peters, C. Mendis, S. Muller, and N. Hort, *JOM* 68, 1183 (2016).
7. J. Qiao, F.B. Bian, M. He, and Y. Wang, *Trans. Nonferrous Met. Soc. China* 23, 2857 (2013).
8. A. Staroselsky and L. Anand, *Int. J. Plast.* 19, 1843 (2003).
9. J.C. Li, Z.L. He, P.H. Fu, Y.J. Wu, L.M. Peng, and W.J. Din, *Mater. Sci. Eng. A* 651, 745 (2016).
10. J.C. Yu, Z. Liu, Y. Dong, and Z. Wang, *J. Magn. Alloy* 3, 134 (2015).
11. Q.Z. Liu, X.F. Ding, Y.P. Liu, and X.J. Wei, *J. Alloys Compd.* 690, 961 (2017).
12. R. Alizadeh, R. Mahmudi, P.H.R. Pereira, Y. Huang, and T.G. Langdon, *Mater. Sci. Eng. A* 682, 577 (2017).
13. E. Onorbe, G. Garces, P. Perez, and P. Adeva, *J. Mater. Sci.*, 47,1085 (2012).
14. K.Hagihara, A.Kinoshita, Y.Sugino, M.Yamasaki, Y. Kawamura, H.Y. Yasuda, and Y. Umakoshi, *Acta Metall.*, 58, 6282 (2010).
15. K. Hagihara, M. Honnami, R. Matsumoto, *Mater. Trans.*, 61, 2065 (2013).
16. M. Yamasaki, K. Hagihara, S. Inoue, J.P. Hadorn, and Y. Kawamura, *Acta Metall.*, 61, 2065 (2013).
17. Z.R. Zhang, X.Y. Yang, Z.Y. Xiao, J. Wang, D.X. Zhang, C.M. Liu, and T. Sakai, *Mater. Des.* 97, 25 (2016).
18. H.C. Xiao, S.N. Jiang, B. Tang, W.H. Hao, Y.H. Gao, Z.Y. Chen, and C.M. Liu, *Mater. Sci. Eng. A*, 628, 311(2015).
19. C. Xu, T. Nakata, X.G. Qiao, M.Y. Zheng, K. Wu, and S. Kamado, *Sci. Rep.* 7, 40846 (2017).
20. X.J. Zhou, C.M. Liu, Y.H. Gao, S.N. Jiang, X.Z. Han, and Z.Y. Lu, *Metall. Mater. Trans. A* 48, 3060 (2017).
21. X.S. Xia, Q. Chen, J.P. Li, D.Y. Shu, C.K. Hu, S.H. Huang, and Z.D. Zhao, *J. Alloys Compd.* 610, 203 (2014).
22. S.N. Jiang, C.M. Liu, and H.Z. Li, et al., *J. Cent. South Univ. Sci. Technol* 35, 935 (2004).
23. X.J. Zhou, C.M. Liu, Y.H. Gao, S.N. Jiang, W.H. Liu, and L.W. Lu, *J. Alloys Compd.* 724, 528 (2017).
24. C.M. Sellars and W.J. McTegart, *Acta Metall.* 14, 1136 (1966).
25. L. Chen, G.Q. Zhao, and J.Q. Yu, *Mater. Des.* 74, 25 (2015).
26. T.Y. Kwak, H.K. Lim, and W.J. Kim, *Mater. Des.* 644, 645 (2015).
27. M. Sarebanzadeh, R. Mahmudi, and R. Roumina, *Mater. Sci. Eng. A* 637, 155 (2015).
28. Y.H. Kong, P.P. Chang, Q. Li, L.X. Xie, and S.G. Zhu, *J. Alloys Compd.* 622, 738 (2015).
29. Z.H. Du, S.S. Jiang, and K.F. Zhang, *J. Alloys Compd.* 86, 464 (2015).
30. S.W. Zeng, A.M. Zhao, H.T. Jiang, and Y.S. Ren, *J. Alloy. Compd.* 698, 786 (2017).
31. C.M. Sellars and J.A. Whiteman, *Metal. Sci.* 13, 187 (1979).
32. J.M. Yu, Z.M. Zhang, Q. Wang, X.Y. Yin, J.Y. Cui, and H.N. Qi, *J. Alloys Compd.* 704, 382 (2017).
33. Y.V.R.K. Prasad and S. Sasidhara, *ASM International* (OH: Materials Park, 1997).
34. Y.V.R.K. Prasad, H.J. Gegel, S.M. Doraivelu, J.C. Malas, J.T. Morgan, L.A. Lark, et al. *Metall. Mater. Trans. A*, 15A, 1883 (1984).
35. W.W. Peng, W.D. Zeng, Q.J. W, H.Q. Yu, *Mater. Sci. Eng. A*, 571,116 (2013).
36. X.S. Xia, Q. Chen, K. Zhang, Z.D. Zhao, M.L. Ma, and X.G. Li, et al, *Mater. Sci. Eng. A*, 587, 283(2013).
37. W.C. Xu, X.Z. Jin, D.B. Shan, and B.X. Chai, *J. Alloys Compd.* 692, 309 (2017).
38. Y.Y. Zong, D.S. Wen, Z.Y. Liu, and D.B. Shan, *Mater. Des.* 91, 321 (2016).

Publisher's Note Springer Nature remains neutral with regard to jurisdictional claims in published maps and institutional affiliations.